BIOENGINEERING

# Iron oxide nanoparticles augment the intercellular mitochondrial transfer–mediated therapy

**Ting Huang[1†], Tianyuan Zhang[1,2*†], Xinchi Jiang[1,2], Ai Li[1], Yuanqin Su[1], Qiong Bian[1], Honghui Wu[1], Ruyi Lin[1], Ni Li[3], Hongcui Cao[4], Daishun Ling[5], Jinqiang Wang[1], Yasuhiko Tabata[6], Zhen Gu[1*], Jianqing Gao[1,2,7*]**

Copyright © 2021 The Authors, some rights reserved; exclusive licensee American Association for the Advancement of Science. No claim to original U.S. Government Works. Distributed under a Creative Commons Attribution NonCommercial License 4.0 (CC BY-NC).

**The transfer of mitochondria between cells has recently been revealed as a spontaneous way to protect the injured cells. However, the utilization of this natural transfer process for disease treatment is so far limited by its unsatisfactory transfer efficiency and selectivity. Here, we demonstrate that iron oxide nanoparticles (IONPs) can augment the intercellular mitochondrial transfer from human mesenchymal stem cells (hMSCs) selectively to diseased cells, owing to the enhanced formation of connexin 43–containing gap junctional channels triggered by ionized IONPs. In a mouse model of pulmonary fibrosis, the IONP-engineered hMSCs achieve a remarkable mitigation of fibrotic progression because of the promoted intercellular mitochondrial transfer, with no serious safety issues identified. The present study reports a potential method of using IONPs to enable hMSCs for efficient and safe transfer of mitochondria to diseased cells to restore mitochondrial bioenergetics.**

## INTRODUCTION

Mitochondria, well known as the powerhouse of eukaryotic cells, play a fundamental role in maintaining cellular homeostasis and cellular functions and largely determine cell survival and cell death (*1*). Accumulating evidence has demonstrated that many degenerative diseases, such as pulmonary disease, cardiomyopathy, and brain damage, are tightly linked to mitochondrial dysfunction (*2*–*5*). Therefore, artificial replenishment of the damaged mitochondria in diseased cells with healthy mitochondria to maintain mitochondrial homeostasis has been proposed as an intriguing reparative strategy (*3*, *6*). However, such strategy faces the challenge of conserving mitochondrial integrity during the isolation procedure and exposure in an extracellular environment after isolation (*6*, *7*). Thus, the intercellular mitochondrial transfer has currently gained increasing attention as an enchanting alternative (*8*). Several recent studies have revealed this cellular property that mitochondria are actively delivered from healthy cells to injured cells under disease stress (*3*, *4*, *9*). Nonetheless, the efficiency of this process cannot meet the high demands of reversing mitochondrial dysfunction (*10*, *11*). Moreover, selective transfer of mitochondria to diseased cells is another challenge for the therapeutic applications of this process, with related safety issues. Consequently, a quick and targeting intercellular transfer of mitochondria to diseased cells is highly desirable for an immediate and safe restructuring of mitochondrial homeostasis to decrease cellular apoptosis, promote cell survival, and recover cell functions (*12*).

In this regard, mesenchymal stem cells (MSCs) are emerging as potential mitochondrial donor cells (*3*, *6*, *13*, *14*), partly because the fewer energy demands of MSCs in the glycolytic state benefit mitochondrial transfer to diseased cells, where they usually have high bioenergetic needs (*15*). Moreover, MSCs have a remarkable homing capability toward diseased tissues (*16*–*18*), providing the possibility for a targeted mitochondrial transfer. Thus, these features, together with the immune privilege, low oxidative damage levels, and tightly regulated redox balance of MSCs (*16*, *17*, *19*, *20*), render MSCs as ideal donor cells for selective delivery of diseased cells with healthy mitochondria. Nevertheless, it remains challenging for an efficient mitochondrial replenishment in diseased cells, which determines the therapeutic gains as mentioned above. To this end, we here propose iron oxide nanoparticle (IONP)–based engineering of MSCs for improving their mitochondrial transfer rate between cells. IONPs are regarded as promising biologically tolerated materials for stem cell engineering (*21*). Notably, the unique biological impact of this inorganic nanomaterial on regulating the functional protein expression of MSCs, such as CXC chemokine receptor 4 (CXCR4) (*18*) and connexin 43 (Cx43), has been recently observed (*22*). Specifically, the formation of Cx43-containing gap junction channels (GJCs) is essential for intercellular transfer of mitochondria and largely determines the mitochondrial transfer rate (*3*, *12*, *23*). Hence, the utilization of IONP-based engineering to augment the mitochondrial transfer rate of MSCs could be one option for efficient mitochondrial replenishment of diseased cells.

As a case to show the therapeutic gains of applying IONPs to artificially promote intercellular transfer of mitochondria in reversing disease progression, we investigated the therapeutic effects of IONP-engineered human placental MSC (Fe-hMSC) in the treatment of pulmonary fibrosis (PF). PF is a fatal disease with increasing prevalence and incidence worldwide, while the present treatment strategy encounters the challenges of the limited therapeutic outcomes and severe side effects (*24*–*26*). Moreover, PF is a major complication in coronavirus disease 2019 (COVID-19) evolution. It has been reported that more than one-third of recovered COVID-19

[1]College of Pharmaceutical Sciences, Zhejiang University, Hangzhou 310058, China. [2]Dr. Li Dak Sum and Yip Yio Chin Center for Stem Cell and Regenerative Medicine, Zhejiang University, Hangzhou 310058, China. [3]Department of Cardiothoracic Surgery, Ningbo Medical Center, Lihuili Hospital Affiliated to Ningbo University, Ningbo, Zhejiang 315041, China. [4]State Key Laboratory for Diagnosis and Treatment of Infectious Diseases, the First Affiliated Hospital, School of Medicine, Zhejiang University, Hangzhou 310003, China. [5]School of Chemistry and Chemical Engineering, Frontiers Science Center for Transformative Molecules, National Center for Translational Medicine, Shanghai Jiao Tong University, Shanghai 200240, China. [6]Department of Biomaterials, Field of Tissue Engineering, Institute for Frontier Medical Sciences, Kyoto University, Kyoto, Japan. [7]Westlake Laboratory of Life Sciences and Biomedicine, Zhejiang, China.
*Corresponding author. Email: tianyuanzhang@zju.edu.cn (T.Z.); guzhen@zju.edu.cn (Z.G.); gaojianqing@zju.edu.cn (J.G.)
†These authors contributed equally to this work.

patients have developed PF (*27*, *28*). Therefore, an effective and safe therapeutic intervention for PF is highly desired (*29*). In particular, the present COVID-19 pandemic highlights the significance of prophylactic PF treatment or definitive PF therapies. As several recent studies have revealed that mitochondrial dysfunction is a pathogenic mediator of PF and even pathogenesis for the progression and severity of COVID-19 (*30*–*33*), the mitochondrial replenishment therapy using Fe-hMSCs may provide a potential strategy for PF treatment. The present study showed a significantly improved mitochondrial transfer rate from Fe-hMSCs to injured alveolar epithelial cells (AECs), owing to the overexpression of Cx43 triggered by IONPs. Meanwhile, Fe-hMSCs maintained the preference of selective mitochondrial transfer to injured AECs. As a result, obvious mitigation of PF progression was observed after the mitochondrial replenishment therapy through Fe-hMSCs (Fig. 1).

## RESULTS

### Bioengineering of using IONPs to promote Cx43 expression in hMSCs

Uniform IONPs at a diameter of around 20 nm were synthesized according to our previous reports (*18*, *34*). Transmission electron microscopy (TEM) of the IONPs is demonstrated in Fig. 2A. After the coincubation of these IONPs with hMSCs for 24 hours, a significantly increased Cx43 expression in hMSCs was observed at an IONP concentration of 30 μg $ml^{-1}$ (Fig. 2B; the data of three-time replications are shown in fig. S1; the concentrations of IONPs were calculated according to the iron amount). Increasing the concentration of IONPs could lead to adverse effects on the Cx43 expression levels, probably owing to the increased cytotoxicity (fig. S2A). However, no cytotoxicity was observed at the concentration of 30 μg $ml^{-1}$ (fig. S2B). The effects of IONPs to promote Cx43 expression in hMSCs were further confirmed by the confocal laser scanning microscopy (CLSM) (Fig. 2C). The ferrous ions ($Fe^{2+}$) were more prone to trigger the overexpression of Cx43 compared to the ferric ions ($Fe^{3+}$) (Fig. 2D; the data of three-time replications are shown in fig. S3), suggesting that this effect may be due to the partial degradation of IONPs in cells (*22*). In addition, it was observed that iron ions at the concentration of 10 μg $ml^{-1}$ could trigger the overexpression of Cx43 in hMSC (fig. S4; results of the Western blot analysis for three-time replications are shown in fig. S5). These different required concentrations between iron ions and IONPs for triggering the Cx43 overexpression may be because more IONPs are required for the partial degradation to sufficient concentration of iron ions.

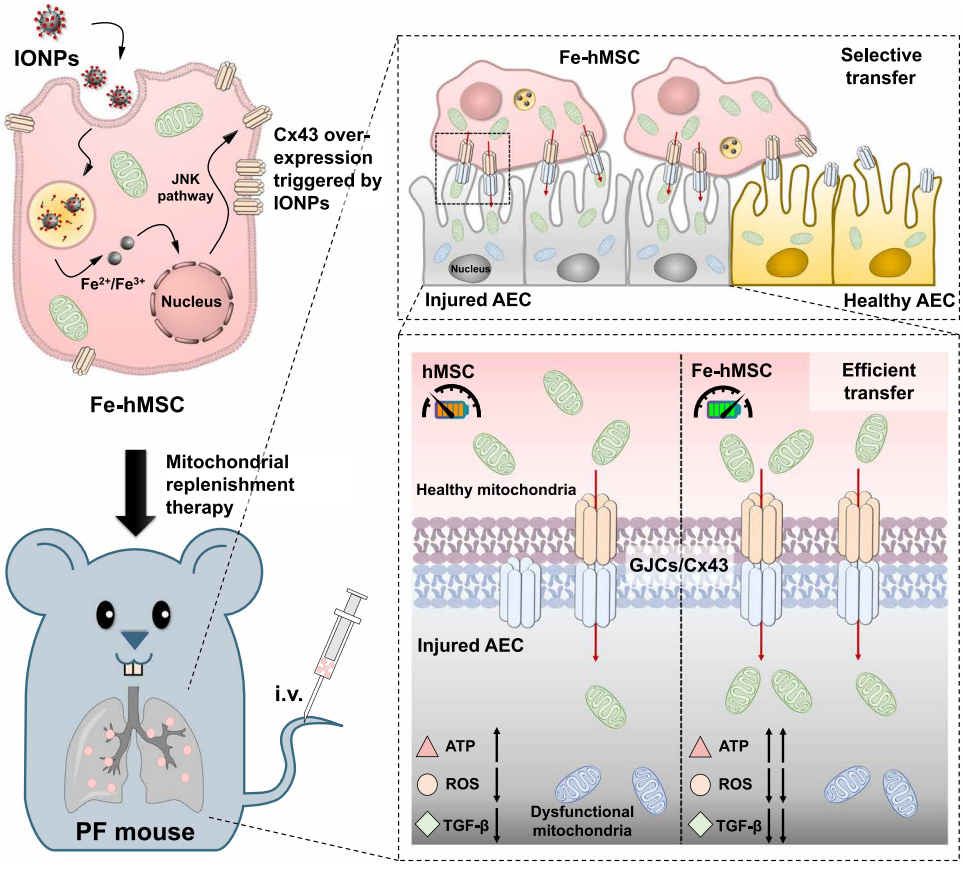


**Fig. 1. Schematic illustration showing a potential strategy of using IONPs to augment the intercellular mitochondrial transfer from hMSCs specialized to injured AECs to prevent the progression of PF.** The cellular uptake of IONPs efficiently triggered the up-regulation of Cx43-containing GJCs of hMSCs, probably through c-Jun N-terminal kinase (JNK) pathway activation. These IONP-activated hMSCs (Fe-hMSCs) demonstrated the ability of transferring their healthy mitochondria to injured AECs selectively with a high transfer rate through the Cx43-containing GJCs, bringing significantly improved therapeutic outcomes in recovering adenosine triphosphate (ATP) levels and decreasing intracellular reactive oxygen species (ROS) and transforming growth factor–β (TGF-β) expression of injured AECs. Consequently, Fe-hMSCs could serve as a living battery of mitochondria to restore the bioenergetics in injured AECs for efficient PF intervention. i.v., intravenous injection.

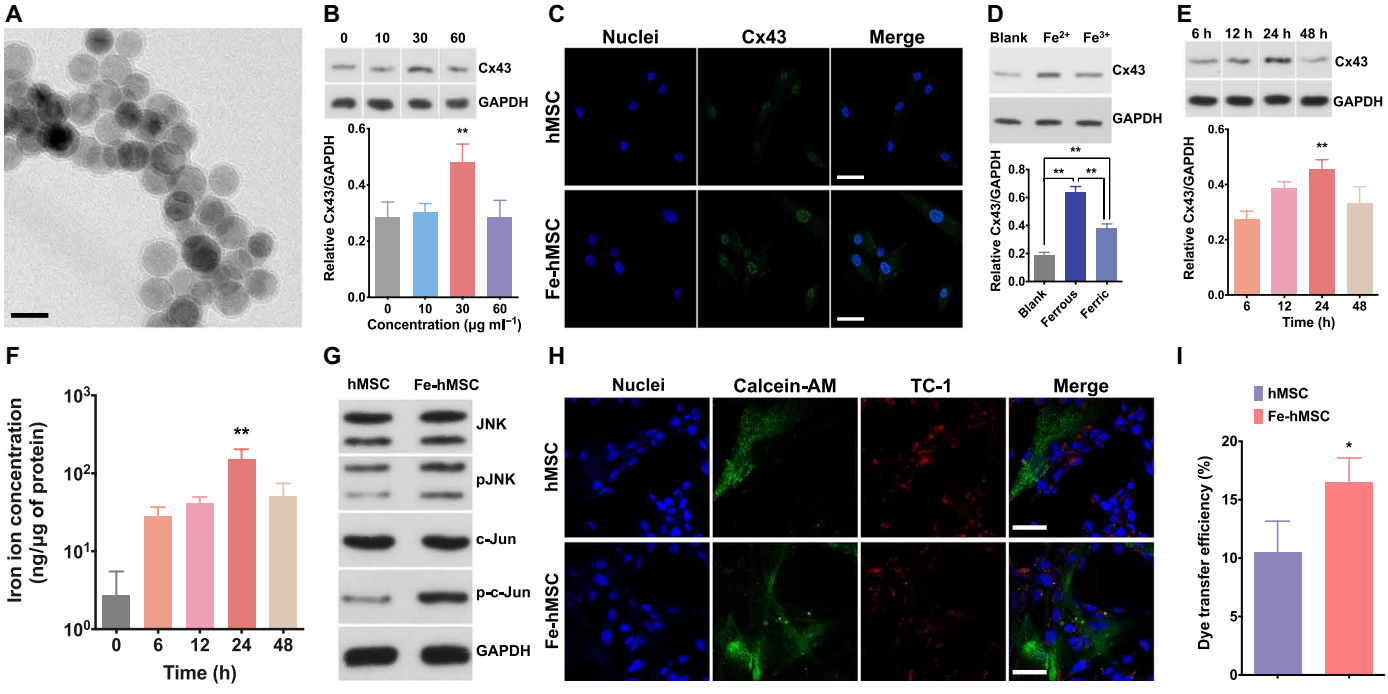


**Fig. 2. IONPs significantly activated Cx43 overexpression in hMSCs.** (**A**) TEM image of the IONPs with hydrophilic surface coating. Scale bar, 20 nm. (**B**) Representative image of Western blot analysis and semiquantification of Cx43 expression after treating hMSCs with IONPs at various concentrations ($n = 3$). (**C**) Fluorescence images indicate Cx43 expression in hMSCs and Fe-hMSCs (IONPs at 30 μg ml$^{-1}$). Blue, nuclei; green, Cx43. Scale bars, 20 μm. (**D**) Representative image and semiquantitative data of Cx43 expression after treating hMSCs with $Fe^{2+}$ or $Fe^{3+}$ at the iron concentration of 30 μg ml$^{-1}$ assessed by Western blot analysis. hMSCs without any iron ion treatment were regarded as the blank group. The Cx43 expression levels among these groups were compared ($n = 3$). (**E**) Representative image of Western blot analysis and semiquantification of Cx43 expression in hMSCs at the indicated time points ($n = 3$). (**F**) Concentrations of iron ions in hMSCs at the indicated time points after the IONPs uptake ($n = 4$). (**G**) The intracellular signaling cascades of JNK pathway of hMSCs and Fe-hMSCs were assessed by Western blot analysis. (**H**) Intercellular transfer of calcein-AM from hMSCs to TC-1 cells observed by CLSM (blue, nuclei of cocultured hMSCs and TC-1 cells; green, calcein-AM; red, TC-1 cells). Scale bars, 20 μm. (**I**) Quantitative evaluation of intercellular dye transfer efficiency of calcein-AM from hMSCs or Fe-hMSCs toward TC-1 cells assessed by flow cytometry ($n = 3$). Data are presented as means ± SD (B, D to F, and I). Statistical significance was calculated using ordinary one-way analysis of variance (ANOVA) (B and D to F) and unpaired Student's *t* test (I). *$P < 0.05$ and **$P < 0.01$.

TEM observations further confirmed that the endocytosed IONPs were mainly retained in endosomes (fig. S6A), which have a characteristic low pH environment (pH 4) (*35*). An in vitro study using a conditional medium (pH 4) to resemble endosomes demonstrated that the IONPs in pH 4 solution became more transparent than those in pH 7 solution after 24 hours of incubation (fig. S6B), indicating partial ionization of IONPs into $Fe^{2+}$ or $Fe^{3+}$ ions after endosomal uptake. Moreover, the highest Cx43 expression levels in hMSCs were observed at 24 hours after the initial cellular uptake of IONPs (Fig. 2E; the data of three-time replications are shown in fig. S7). This variation of Cx43 expression levels in hMSCs was consistent with the changes of the degraded iron ion concentrations in hMSCs (Fig. 2F), which further confirmed the correlation of the Cx43 overexpression with IONP degradation. c-Jun N-terminal kinase (JNK) phosphorylation and c-Jun phosphorylation in hMSCs were then examined using Western blots. In addition, an obvious up-regulation in the phosphorylated protein forms of JNK (p-JNK) and c-Jun (p-c-Jun) was observed (Fig. 2G; the original images are shown in fig. S8). These results suggest that IONPs may trigger Cx43 expression through the JNK pathway, which is consistent with previous studies (*22*, *36*). Such overexpression of Cx43 was also observed after treatments with our previously reported ferrimagnetic iron oxide nanochains (MFION; 25-nm-sized nanocubes) (*18*) and the commercial superparamagnetic iron oxide nanoparticle (SPION) product (purchased from Shanghai Aladdin Bio-Chem Technology; 10-nm-sized nanoparticles) (figs. S9 and S10), suggesting that this effect can be widely induced by IONPs with different sizes, shapes, magnetic properties, and surface coatings. Moreover, no detrimental impacts on the quality and biofunction of mitochondria were observed after treating hMSCs with IONPs (fig. S11). In addition, the IONP treatment showed a reduced adverse impact on both the cell viability and the intracellular adenosine triphosphate (ATP) levels of hMSCs in comparison with the direct treatment with ferrous ions or ferric ions at the iron concentrations over 30 μg ml$^{-1}$ (fig. S12).

Because Cx43 has been proved to play a critical role in the intercellular gap junction coupling and gap junctional communication (*37*), the Cx43 overexpression was further investigated to identify whether it would generate a more efficient GJC function of Fe-hMSCs with adjacent mouse AECs (TC-1 cells) and enhance the transportation of cellular contents. Calcein-AM, which can only pass through GJCs, was applied to indicate intercellular transfer. Both CLSM imaging and flow cytometry analysis showed a more efficient transfer of biomolecules from Fe-hMSCs to TC-1 cells through GJCs (Fig. 2, H and I). However, the IONPs in Fe-hMSCs were not transferred to the cocultured TC-1 cells (fig. S13). Collectively, IONPs have unique effects of triggering Cx43 expression through the JNK pathway, thereby promoting the intercellular transfer of cellular contents through GJCs.

### IONPs augment the mitochondrial transfer from hMSCs to diseased cells selectively

Intercellular transfer of mitochondria from hMSCs to healthy TC-1 cells or injured TC-1 cells (induced by bleomycin treatments, BLM-TC-1) was investigated to determine the capability of hMSCs to transfer mitochondria as mitochondrial donor cells. Flow cytometry analysis showed an extremely low mitochondrial transfer rate from hMSCs to healthy TC-1 cells, while BLM-TC-1 cells received a significantly higher number of mitochondria from hMSCs (Fig. 3A), indicating that hMSCs have the capability of selectively donating their mitochondria to injured cells. Moreover, only the coculture systems achieved a relatively high mitochondrial transfer rate (Fig. 3B), suggesting the GJCs between adjacent cells may play a critical role in determining the transfer rate. Hence, Fe-hMSCs probably promoted

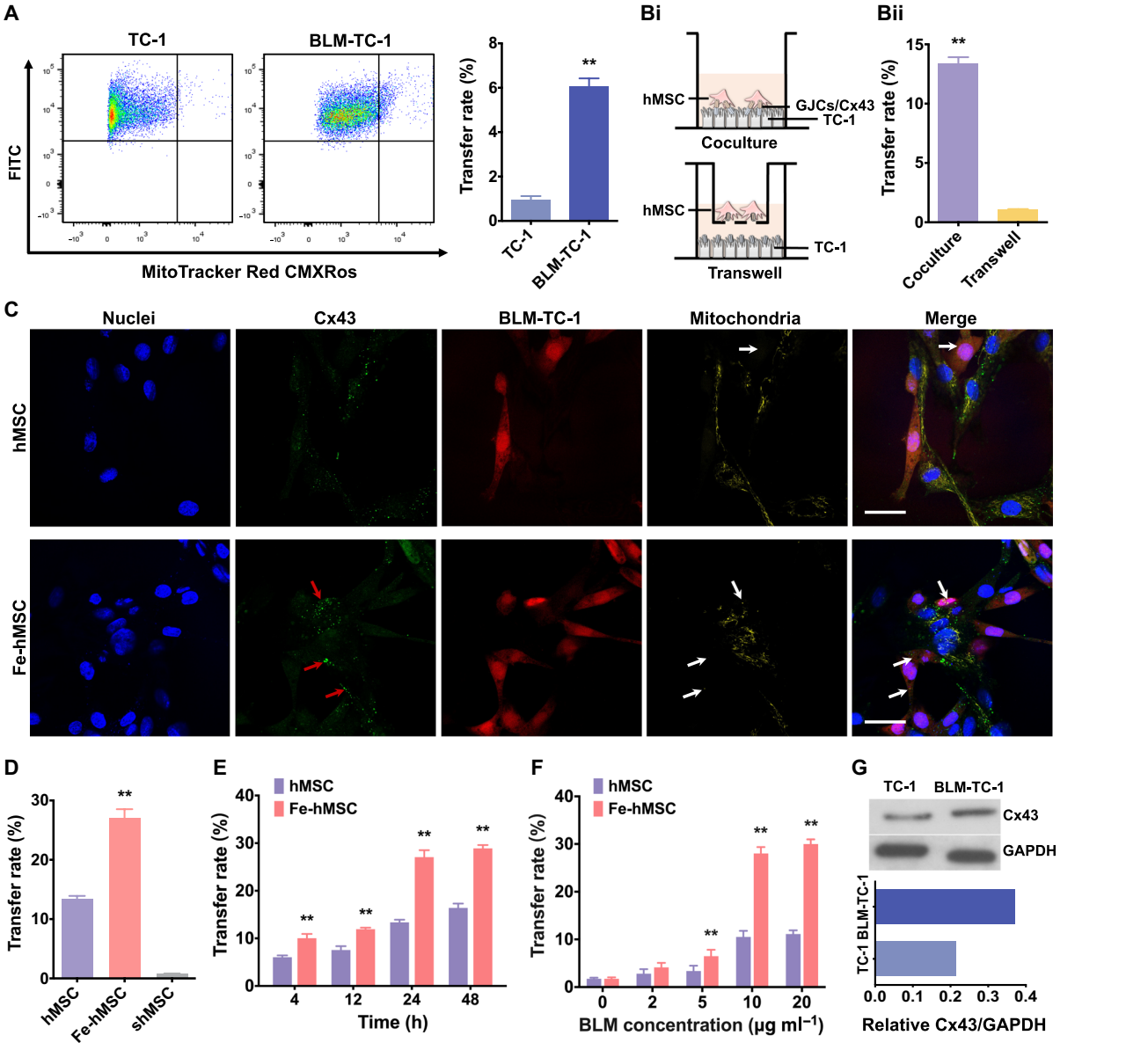


**Fig. 3. IONPs significantly augmented intercellular mitochondrial transfer rates.** (**A**) Mitochondrial transfer rates from hMSCs to TC-1 and BLM-TC-1 cells were compared by assessing labeled mitochondria of hMSCs in GFP-expressing TC-1 cells or BLM-TC-1 cells using flow cytometry. The right panel shows quantitative data of the left panel ($n = 3$). (**B**) Comparison of mitochondrial transfer rate between the coculture system and Transwell system. (Bi) Schematic illustration showing the coculture system and Transwell system. (Bii) Quantitative data on the transfer rates of two types of cell culture systems ($n = 3$). (**C**) CLSM images of Cx43 expression and its relationship with the intercellular transfer of mitochondria from hMSCs or Fe-hMSCs to BLM-TC-1 cells. Red arrows indicate Cx43 expression localized in the transferred mitochondria; white arrows indicate the transferred mitochondria. Scale bars, 20 μm. (**D**) Quantitative comparison of mitochondrial transfer rates of hMSCs, Fe-hMSCs, and shMSCs to BLM-TC-1 cells after a 24-hour coculture ($n = 3$). (**E**) Mitochondrial transfer rates of hMSCs and Fe-hMSCs at the indicated time points following coculture with BLM-TC-1 cells ($n = 3$). (**F**) Mitochondrial transfer rate from hMSCs and Fe-hMSCs to TC-1 cells treated with different concentrations of BLM ($n = 3$). (**G**) Cx43 expression levels of TC-1 cells with or without BLM treatments assessed by Western blot analysis. Semiquantitative data of the top panel are shown in the bottom panel. Data are presented as means ± SD (A, B, and D to F). Statistical significance was calculated using unpaired Student's *t* test (A and B), ordinary one-way ANOVA (D), and ordinary two-way ANOVA (E and F). $^{**}P < 0.01$.

mitochondrial transfer between adjacent cells by activating the formation of Cx43-containing GJCs. To verify this assumption, mitochondrial transfer from both hMSCs and Fe-hMSCs toward BLM-TC-1 cells was studied by CLSM. An obviously augmented mitochondrial transfer of Fe-hMSCs, closely related to the Cx43 expression levels, was visualized (Fig. 3C). Thus, these results showed that IONPs had the potential to significantly promote the mitochondrial transfer from Fe-hMSCs to injured TC-1 cells. The dynamic observations of the above intercellular mitochondrial transfer are shown in fig. S14 and movies S1 and S2. Next, quantitative comparisons of mitochondrial transfer rates between hMSCs and Fe-hMSCs were performed, in which Fe-hMSCs showed an approximate twofold increase in mitochondrial transfer rates. In particular, a significantly inhibited mitochondrial transfer was observed after the down-regulation of Cx43 expression in hMSCs (shMSCs) (Fig. 3D), prepared through small interfering RNA (siRNA) transfection (fig. S15). These results strongly suggest the prominent role of Cx43-containing GJCs in regulating the intercellular transfer rate of mitochondria. Moreover, the transfer rates were continuously increased after the initial coincubation at the first 24 hours and maintained at the second 24 hours (Fig. 3E), consistent with previous Cx43 expression tests (Fig. 2E). The transfer rate of mitochondria is related to the injury degrees of TC-1 cells, and significant intercellular mitochondrial transfers were observed when the viability of TC-1 cells was below 50% (Fig. 3F and fig. S16). In addition, such selected mitochondrial transfer could also be observed in the mitochondria dysfunctional TC-1 cells induced by carbonyl cyanide 3-chlorophenylhydrazone (CCCP), a typical mitochondrial phosphoric acid oxide–dissolving coupling agent, showing that this ability of hMSCs involved multiple types of injured cells (fig. S17; the original data of Western blot analysis were shown in fig. S18). Notably, the injury inducement using bleomycin (BLM) also up-regulated the Cx43 expression in TC-1 cells, which further benefited the selective and efficient mitochondrial transfer toward BLM-TC-1 cells through Cx43-containing GJCs (Fig. 3G). This is because the formation of GJCs between cells requires both high expression of connexins of the adjacent cells (*38*, *39*). It was further observed that the Cx43 expression levels in TC-1 and BLM-TC-1 cells were also increased after coculture with hMSCs or Fe-hMSCs, and coculture with Fe-hMSCs induced higher Cx43 expression levels in TC-1 and BLM-TC-1 cells than in hMSCs (fig. S19; the original data of the Western blot analyses were shown in fig. S18). These enhanced Cx43 expression levels in TC-1 cells after coculture may be due to the augmented GJCs induced by Fe-hMSCs. We then examined mitochondrial transfer from injured TC-1 cells to hMSCs or Fe-hMSCs, suggesting a bidirectional mitochondrial transfer between hMSCs/Fe-hMSCs and injured TC-1 cells (fig. S20). However, the transfer rate from injured TC-1 cells to hMSCs was much lower than that from hMSCs to injured TC-1 cells, probably due to the high oxidative energy demands of dysfunctional mitochondria (*20*).

### IONPs assisted hMSCs to restore injured cells through efficient intercellular transfer of mitochondria

The initiation and progression of PF are closely related to mitochondrial dysfunction of AECs (*33*). An impaired mitochondrial function reduces the efficiency of the electron transport chain, resulting in dysregulated ATP metabolism and increased production of reactive oxygen species (ROS). The cumulative imbalanced ROS levels and endoplasmic reticulum stress responses further promote activation of the fibrotic signaling pathway, leading to irreversible fibrosis (*30*). In this regard, the improved mitochondrial transfer capability of Fe-hMSCs may provide an opportunity to immediately restore mitochondrial functions and maintain intracellular ROS balance, which conspicuously suspends the fibrotic process. To prove this, mitochondrial functions of injured TC-1 cells after different treatments were first evaluated.

As demonstrated in Fig. 4A, the mitochondrial membrane potential of TC-1 cells markedly decreased after BLM treatments. Only hMSCs, Fe-hMSCs, and free mitochondria isolated from hMSCs (hMSC-mito) could restore the mitochondrial membrane potential to some extent. However, the hMSCs cultured in the Transwell system (Trans-hMSCs), shMSCs, and mitochondrial DNA (mtDNA)–depleted hMSCs (de-hMSCs; fig. S21) showed an inability to restore the mitochondrial membrane potential. Similar results were observed in restoring intracellular ATP levels (Fig. 4B), mitochondrial ROS levels (Fig. 4C), and cellular proliferation rate (Fig. 4D). In particular, the treatment with Fe-hMSCs almost fully restored the injured TC-1 cells in terms of their cellular proliferation rate and ROS level, showing no statistical differences in the comparison with the healthy control group. These results suggest that the efficient mitochondrial transfer ability of Fe-hMSCs enabled the restoration of mitochondrial functions and assisted in the rebalancing of mitochondrial redox homeostasis. Compared with hMSCs, Fe-hMSCs exhibited efficient mitochondrial replenishability to quickly reverse mitochondrial dysfunction, leading to a marked decrease in cellular apoptosis (Fig. 4E). Fe-hMSC treatment led to healthier mitochondria in BLM-TC-1 cells than hMSC treatment (fig. S22). As a result, Fe-hMSC treatment was more effective in promoting cell viability than hMSC treatment (Fig. 4F). In addition, Fe-hMSCs even achieved much higher cell survival in the treated cells than isolated mitochondria and had no statistical difference in comparison with the healthy control group, probably because of the paracrine actions (*40*). Subsequently, we assessed the transforming growth factor–β (TGF-β) expression of injured TC-1 cells induced by BLM. TGF-β expression is a classical fibrotic signal followed by mitochondrial dysfunction (*30*, *41*). Western blot analysis showed that Fe-hMSCs achieved the best inhibition of TGF-β expression. However, silencing Cx43 expression or depleting mtDNA led to the dysfunction of hMSCs in inhibiting TGF-β expression (Fig. 4G; the original images are shown in fig. S23, and the semiquantitative data are presented in fig. S24). Unlike other assessments described above, TGF-β expression of hMSCs in the coculture system and Transwell system showed similar levels, which could be attributed to the therapeutic paracrine actions of hMSCs (*40*, *42*, *43*).

### IONP-augmented intercellular mitochondrial transfer of hMSCs remarkably mitigated the progression of PF

So far, we have demonstrated the potential of IONPs in assisting an efficient and selective mitochondrial replenishment through Fe-hMSCs to restore the BLM-TC-1 cells in in vitro studies. The therapeutic ability of these IONP-reinforced hMSCs was subsequently investigated in a mouse PF model induced by intratracheal BLM according to previous studies (*33*, *44*). Fe-hMSCs were administered through the tail vein on the next day after the intratracheal administration of BLM. The therapeutic period lasted for 28 days (Fig. 5A). Distribution studies demonstrated good homing with long-term retention of systemically administered Fe-hMSCs in the fibrotic lung compared with the healthy lung or intratracheal phosphate-buffered solution

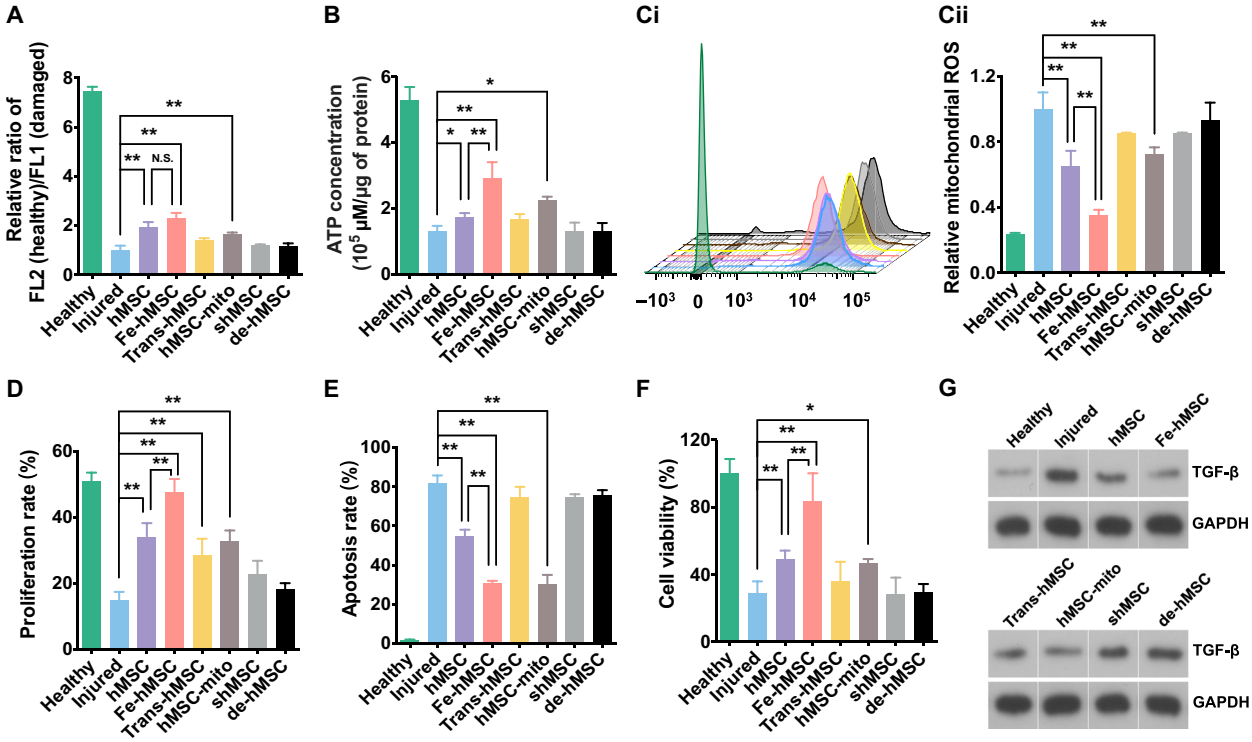


**Fig. 4. IONPs improved the therapeutic ability of hMSCs to restore injured cells.** (**A**) Mitochondrial membrane potentials of TC-1 cells after the indicated treatments assessed by comparing the ratio of healthy mitochondria to damaged mitochondria ($n = 3$). (**B**) Intracellular ATP levels of TC-1 cells after the indicated treatments ($n = 3$). (**C**) Relative mitochondrial ROS levels of TC-1 cells after the indicated treatments. (Ci) Fluorescence intensity of ROS probe evaluated by flow cytometry. (Cii) Quantitative data of Ci ($n = 3$). (**D**) Proliferation rates of TC-1 cells after the indicated treatments evaluated by the ethynyl deoxyuridine (EdU) cell proliferation detection kit ($n = 3$). (**E** and **F**) Cellular apoptosis and viability of TC-1 cells after the indicated treatments ($n = 3$). (**G**) TGF-β expression levels of TC-1 cells after the indicated treatments. Data are presented as means ± SD (A to F). Statistical significance was calculated using ordinary one-way ANOVA (A to F). $^*P < 0.05$ and $^{**}P < 0.01$. N.S., no significant difference.

(PBS)–treated lung; Fe-hMSCs could exist in the fibrotic lung over 10 days (fig. S25). Pulmonary sections further confirmed the ideal homing capacity of Fe-hMSCs to fibrotic lung (fig. S26). Fe-hMSCs could attach with AECs, providing opportunities for mitochondrial transfer through GJCs. After a 28-day treatment, more than 90% of PF model mice treated with Fe-hMSCs survived. Meanwhile, only 70% of PF model mice and more than 85% of PF model mice treated with hMSCs survived in comparison (Fig. 5B). However, there was no statistical difference between these groups regarding the survival rate in the present observation. The therapeutic intervention in PF by Fe-hMSCs was confirmed by micro–computed tomography (CT) scanning, which showed a limited fibrotic area 28 days after the intratracheal administration of BLM (Fig. 5C). Moreover, hematoxylin and eosin (H&E) staining and Masson's trichrome staining demonstrated the therapeutic advantages of Fe-hMSCs in mitigating fibrotic progression (Fig. 5Di). Semiquantitative calculation of the fibrotic area further showed significantly improved therapeutic gains using Fe-hMSCs, which had no statistical difference in comparison with the healthy control group regarding the fibrotic area (Fig. 5Dii). Moreover, analysis of the bronchoalveolar lavage fluid (BALF) presented significantly decreased TGF-β and matrix metalloproteinase 9 (MMP9) expressions after treatment with Fe-hMSCs than with hMSCs (Fig. 5, E and F). However, the expression levels were still significantly higher compared to the healthy control group. TEM observations of pulmonary sections showed more healthy mitochondria in the injured epithelia after treatment with Fe-hMSCs, with no statistical difference compared to the healthy epithelia (Fig. 5G and fig. S27), indicating that the above therapeutic outcomes were probably due to mitochondrial rescue through the replenishment therapy. Furthermore, biochemical detections of the superoxide dismutase (SOD), malondialdehyde (MDA), and hydroxyproline in pulmonary samples also demonstrated the advantages of Fe-hMSCs in restoring the antioxidant ability of diseased AECs and preventing fibrotic progression compared with hMSCs (Fig. 5, H to J). In addition, there was no significant difference between the Fe-hMSC treatment group and the healthy control group regarding the hydroxyproline content. Preliminary safety evaluations showed limited risks of mitochondrial replenishment therapy using Fe-hMSCs (figs. S28 and S29). Besides, the administration of Fe-hMSCs on 7 or 14 days after intratracheal administration of BLM showed a reduced ability to mitigate PF progression (fig. S30).

## The highly efficient mitochondrial transfer ability of hMSCs triggered by IONPs contributed to the mitigation of PF progression

We then investigated the critical role of augmented intercellular mitochondrial transfer triggered by IONPs in mitigating PF progression. Pulmonary sections observed using CLSM showed the transfer of mitochondria (stained in red) from green fluorescent protein (GFP)–expressed hMSCs or Fe-hMSCs (labeled in green) to CK7 antibody-labeled AECs (stained in purple), indicating intercellular mitochondrial transfer in fibrotic lungs (Fig. 6A). Notably,

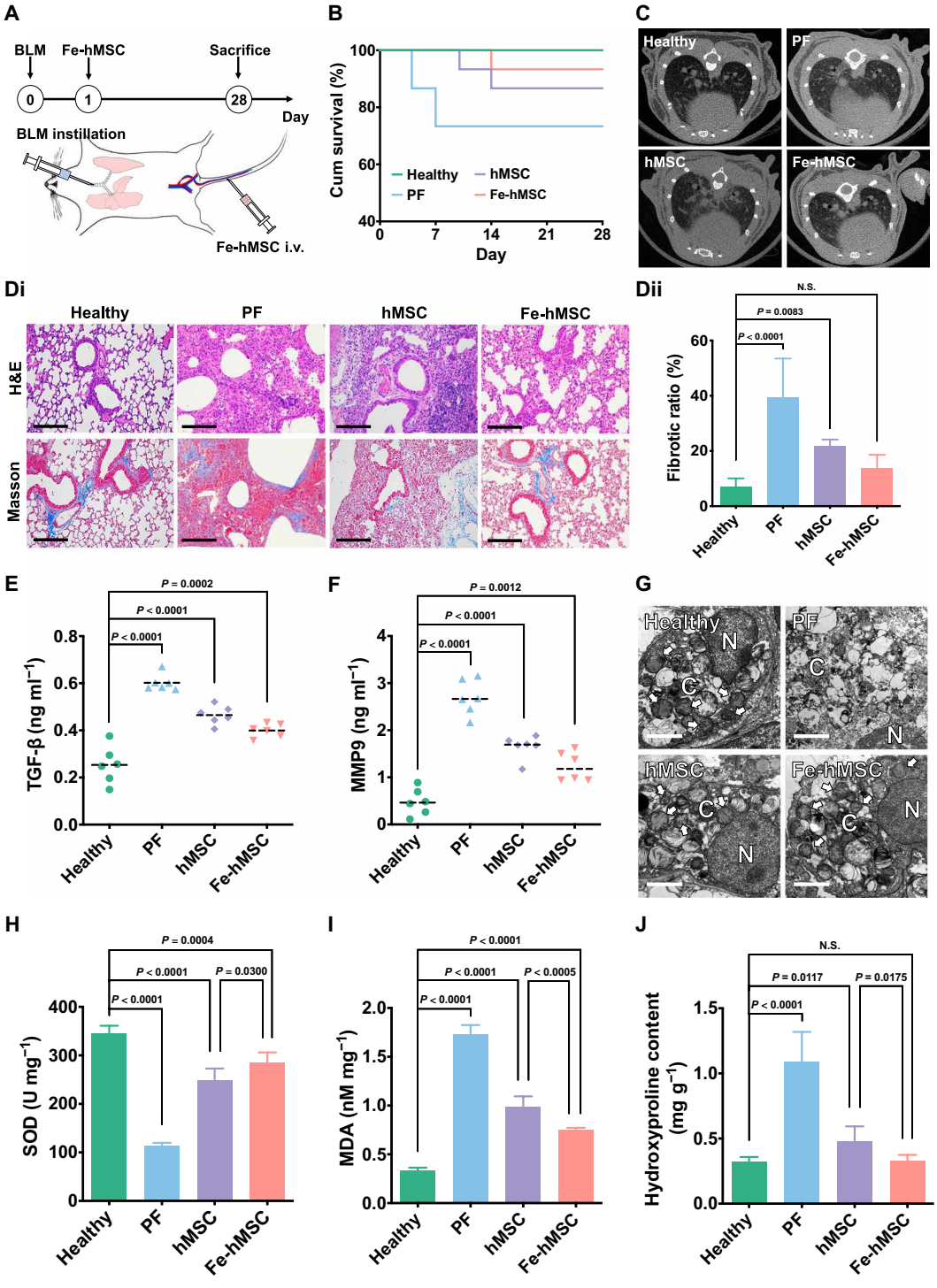


**Fig. 5. The augmented mitochondrial transfer by using IONPs attributed to an efficient intervention of PF progression.** (**A**) Schematic illustration showing therapeutic evaluations. Intratracheal BLM was administered to C57BL/6 mice to induce PF. Therapeutic $5 \times 10^5$ hMSCs were systemically administered through the tail vein on the next day after BLM-induced injury. Curative evaluations were conducted on day 28. (**B**) Kaplan-Meier survival curves of fibrotic mice with various treatments ($n = 15$). (**C**) Micro-CT images of mice lungs after various treatments on day 28. (**D**) Pathological examination of recipient mice pulmonary sections. (Di) Representative images of H&E staining and Masson's trichrome staining of pulmonary sections. Scale bars, 100 μm. (Dii) Quantitative data of the fibrotic area calculated from pulmonary sections using Masson's trichrome staining using ImageJ ($n = 6$). (**E** and **F**) Amount of TGF-β and MMP9 in the collected BALF ($n = 6$). (**G**) TEM images of AECs after the indicated treatments. N refers to the cell nucleus, and C refers to the cytoplasm. Scale bars, 2 μm. (**H** to **J**) Levels of SOD, MDA, and hydroxyproline in lung homogenates ($n = 5$). Data are presented as means ± SD (D and H to J) and means with scatter dot plot (E and F). Statistical significance was calculated using log-rank test (B) and ordinary one-way ANOVA (D to F and H to J).

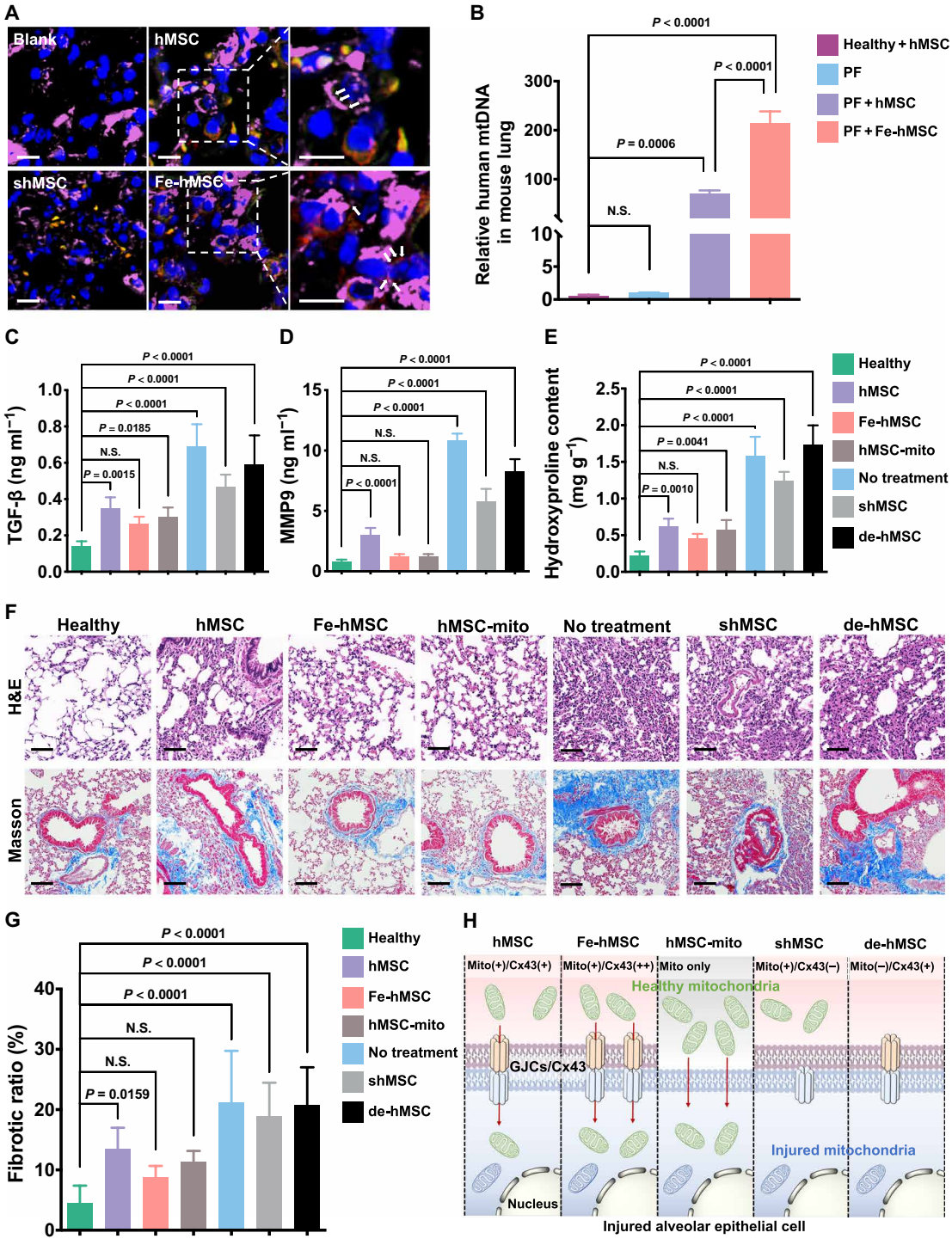


**Fig. 6. The mitochondrial transfer rate determines the therapeutic efficiency against PF progression.** (**A**) Representative images of recipient mice pulmonary sections after immunofluorescence staining. The transferred mitochondria originating from hMSCs or Fe-hMSCs are indicated by white arrows. (Blue, nuclei; green, hMSCs, Fe-hMSCs, and shMSCs; red, mitochondria of hMSCs or Fe-hMSCs; purple, AECs). Scale bars, 10 μm (left); 5 μm (right). (**B**) Relative amount of human mtDNA in isolated AECs ($n = 3$). (**C** and **D**) Amount of TGF-β and MMP9 in collected BALF after the indicated treatments ($n = 6$). (**E**) Hydroxyproline content in lung homogenates after the indicated treatments ($n = 3$). (**F**) Representative images of H&E-stained and Masson's trichrome–stained pulmonary sections after the indicated treatments. Scale bars, 100 μm. (**G**) Quantitative analysis of the fibrotic area according to the above Masson's trichrome staining was conducted in ImageJ ($n = 6$). (**H**) Schematic figure illustrating that the efficiency of the current therapeutic strategy is closely related to the mitochondrial transfer rate through Cx43-containing GJC approach. Data are presented as means ± SD (B to E and G). Statistical significance was calculated using ordinary one-way ANOVA (B to E and G).

Fe-hMSCs showed more transferred mitochondria than hMSCs, and rare transfer of mitochondria was detected after treatment with shMSCs, indicating the vital role of Cx43 expression in in vivo mitochondrial transfer. These results were further substantiated by measuring human mtDNA in separated mice AECs by polymerase chain reaction (PCR) analysis (Fig. 6B). Furthermore, by assessing the indicators associated with fibrosis, including TGF-β (indicating inflammatory reactions), hydroxyproline (indicating collagen formation), and MMP9 (indicating abnormal epithelial repair processes), Fe-hMSCs showed superiority in impeding fibrotic progression, which was comparable or even slightly better than the free mitochondria and much better than hMSCs. Silencing Cx43 expression (shMSC) or depleting mtDNA of hMSC (de-hMSC) impeded the therapeutic outcomes of hMSCs, especially de-hMSCs (Fig. 6, C to E), consistent with previous in vitro tests (Fig. 4). Moreover, mice pulmonary sections were examined after H&E staining and Masson's trichrome staining, and the fibrotic areas were calculated (Fig. 6, F and G). Similarly, Fe-hMSCs showed slightly and significantly better therapeutic gains against PF progression compared to free mitochondria (hMSC-mito) and hMSCs, respectively. However, this therapeutic capability of hMSCs was interrupted after Cx43 silencing (shMSC) or mtDNA depletion. Together, we show that the up-regulated Cx43 expression in hMSCs via IONPs can affect the intercellular mitochondrial transfer rate and consequently determines the therapeutic efficiency against PF progression (Fig. 6H).

## DISCUSSION

Regardless of the naturally occurred process to protect and rescue the diseased cells via intercellular transfer of mitochondria from health cells to diseased cells (*3*, *13*, *45*), the efficiency of this self-repair pathway in most pathological conditions is usually insufficient. For example, astrocytes have been demonstrated to have the ability to spontaneously transfer mitochondria toward neurons for mitigating the damage induced by cerebral ischemia (*4*). Nevertheless, the poststroke recovery still demonstrated a high mortality and a high rate of deformity (*46*). Thereby, the present study aims to potentiate this physiological process of mitochondrial transfer for an efficient mitochondrial replenishment therapy.

We here showed that Cx43-containing GJCs could be another approach for intercellular mitochondrial transfer of hMSCs. We found that the effect of IONPs in promoting mitochondrial transfer between cells could be widely induced by IONPs with different sizes, shapes, magnetic properties, and surface coatings, making this strategy universally applicable for hMSC bioengineering. In addition, compared with the direct use of free iron ions, a strategy using IONPs has the advantages of a less cytotoxicity to hMSCs, which is probably because the partial degradation of IONPs to ions causes a more gradual increase in the iron ion levels than when applying free iron ions.

Another challenge for artificial mitochondrial replenishment therapy is the selective delivery of diseased cells with exogenous mitochondria, which is critical for high therapeutic efficiency and safety. The present study showed that systemically administered Fe-hMSCs have excellent homing ability to fibrotic lungs and long-time retention. Further observation of pulmonary sections showed the attachment of Fe-hMSCs with AECs, which is a prerequisite for mitochondrial transfer through GJCs. Measurement of human-sourced mtDNA in mice AECs showed a significantly higher mitochondrial transfer from hMSCs to fibrotic AECs, indicating the ability of hMSCs to selectively restore diseased cells.

In the therapeutic evaluations against the fibrotic progression, we have demonstrated the advantages of the highly efficient mitochondrial transfer from Fe-hMSCs to injured AECs in mitigating the progression of PF (Fig. 5). However, we are, so far, unable to completely exclude the interference by other therapeutic benefits generated by MSCs. For example, MSCs are known to exert their reparative effects through paracrine actions, which protect AECs against apoptosis and inflammation and promote angiogenesis (*40*, *42*, *43*). This property can further explain the results demonstrated in the present study, in which the Transwell system with a low mitochondrial transfer rate shows comparable levels of TGF-β expressions compared with the coculture system (Figs. 3B and 4G and fig. S24). Nonetheless, the TGF-β expression levels of hMSCs in the two types of culture systems were still much higher than that of Fe-hMSCs, indicating the indispensable role of efficient mitochondrial replenishment in repairing fibrotic lungs. In addition, Fe-hMSCs even showed the ability to treat progressed PF to some extent, while hMSCs demonstrated a relative inability to repair the fibrotic lungs (fig. S30). These advantages of Fe-hMSCs in the treatment of progressed PF further support the idea that the efficient mitochondrial transfer to injured cells can be a promising strategy to treat the diseases caused by mitochondrial dysfunction.

## MATERIALS AND METHODS

### Materials

Benzyl ether (99%), sodium oleate (99%), docosane (99%), polycaprolactone [PCL; average weight-average molecular weight ($M_W$) = 14,000], oleic acid (OA; 90%), eicosane (99%), branched polyethyleneimine [PEI; $M_W$ = 25,000], and 4′,6-diamidino-2-phenylindole (DAPI) were purchased from Sigma-Aldrich Chemical Co. (St. Louis, USA). Iron (III) acetylacetonate (99%) and 4-biphenylcarboxylic acid (95%) were purchased from Acros Organics Co. (Geel, Belgium). Chloroform, ethanol, hexane, tetrahydrofuran, formaldehyde, sodium hydroxide, and concentrated nitric acid were purchased from Sinopharm Chemical Reagent Co. Ltd. (Shanghai, China). SPION with a diameter of 10 nm (U196711), iron (III) chloride, aluminum sulfate octadecahydrate (99%), potassium ferrocyanide trihydrate (99%), and BLM were purchased from Aladdin Co. Ltd. (Shanghai, China). Four percent of paraformaldehyde and mitochondria isolation kit were purchased from Solarbio Science and Technology Co. Ltd. (Beijing, China). Ferric trichloride, ferrous sulfate, ethidium bromide, and uridine were purchased from Macklin Inc. (Shanghai, China). Sodium pentobarbital was purchased from Merck KGaA Co. Ltd. (Darmstadt, Germany). The MesenCult MSC Basal Medium and MesenCult Stimulatory Supplements were purchased from Stemcell Technologies Inc. (Vancouver, Canada). RPMI 1640 and Hanks' balanced salt solution (HBSS) were purchased from Cienry BioTECH Co. Ltd. (Huzhou, China). MitoTracker probes and CM-Dil were purchased from Invitrogen Co. Ltd. (Carlsbad, USA). Dihydroethidium (DHE) probe, MDA, and SOD kit were purchased from Jiangsu KeyGEN BioTECH Co. Ltd. (Nanjing, China). Calcein-AM was purchased from Shanghai YuanYe Biotechnology Co. Ltd. (Shanghai, China). Cx43 antibody was purchased from Boster Bioengineering Co. Ltd. (Wuhan, China). TGF-β, c-Jun, p-c-Jun, and glyceraldehyde phosphate dehydrogenase (GAPDH) antibody were purchased from Abcam plc. (Cambridge, UK). CD31, CD45,

and CD326 antibody were purchased from BioLegend Inc. (San Diego, USA). JNK and p-JNK antibody were purchased from Cell Signaling Technology Inc. (Boston, USA). Cy5-conjugated CK7 antibody was purchased from Proteintech Inc. (Wuhan, China). Tween 20 was purchased from Huadong Medicine Co. Ltd. (Hangzhou, China). Triton X-100 was purchased from Beyotime Biotechnology Co. Ltd. (Shanghai, China). MitoSOX red mitochondrial superoxide indicator and CCCP were purchased from Yeasen BioTECH Co. Ltd. (Shanghai, China). Radioimmunoprecipitation assay (RIPA) buffer, protease inhibitor cocktail, and phenylmethylsulfonyl fluoride were purchased from Servicebio Technology Co. Ltd. (Wuhan, China). Bovine serum albumin (BSA), LipoHigh liposome, sodium pyruvate, rapid blood genomic DNA extraction kit, and the 2xSG Fast qPCR Master Mix (High Rox) kit were purchased from Sangong BioTECH Co. Ltd. (Shanghai, China). The Cx43-siRNA and primers of PCR were synthesized by Sangong BioTECH Co. Ltd. (Shanghai, China).

### Cell culture

hMSCs were obtained following our previously reported protocols (*47*). A special medium composed of human basal medium with 10% of stimulatory supplements was applied to incubate the purified hMSCs. All protocols for human tissue and cell handling were approved by the Research Ethics Committee of First Affiliated Hospital, School of Medicine, Zhejiang University (reference number 2013-272). Mouse AECs (TC-1) were gifted by P. Luo at Zhejiang University. TC-1 cells were maintained in RPMI 1640 with a supplement of 10% fetal bovine serum, penicillin (100 U $ml^{-1}$), and streptomycin (100 μg $ml^{-1}$). TC-1 cell injury was induced by BLM at indicated concentrations (2 to 20 μg $ml^{-1}$) for 24 hours or CCCP (50 μM) for 20 min. All cells were incubated in a humid atmosphere of 5% $CO_2$ at 37°C.

### Bioengineering of hMSCs using IONPs

hMSCs were seeded in culture dishes beforehand for 24 hours. The culture medium was replaced with a serum-free medium for bioengineering. IONPs at indicated concentrations were added to hMSCs for 1 hour of incubation, followed by replacement with fresh serum-containing culture medium for an additional 24 hours of incubation to harvest Cx43-overexpressed hMSCs (Fe-hMSCs).

### Intercellular transfer through GJCs

hMSCs and TC-1 cells were pretreated with calcein-AM and labeled with a fluorescent dye of CM-Dil, respectively. The two types of cells were cocultured for 24 hours before the cell fixation, followed by nuclear staining of DAPI (100 ng $ml^{-1}$). The intercellular transfer of calcein-AM was observed using CLSM (TCS SP8, Leica, Wetzlar, Germany). The transfer rate was further quantitatively evaluated through a BD LSRFortessa cytometer (BD Biosciences, San Jose, USA), in which the dual-positive cells were gated and quantitatively analyzed.

### Assessments of the in vitro mitochondrial transfer

The mitochondrial transfer was observed by CLSM, and the transfer rate was assessed using a flow cytometer. Briefly, hMSCs were incubated in a prewarmed staining solution containing the MitoTracker probe (MitoTracker Red CMXRos, 50 nM) for 30 min. After washing thrice with neutral PBS to remove the free probe, hMSCs were cocultured with mCherry fluorescent protein–expressed TC-1 cells (mCherry-TC-1) for 24 hours. The mCherry-TC-1 cells were prepared by lentivirus transfection according to the manufacturer's instructions (Jikai Gene, Shanghai, China). These cocultured cells were fixed by 4% paraformaldehyde and stained with DAPI and fluorescein isothiocyanate (FITC)–conjugated Cx43 antibody. CLSM was applied to observe the mitochondrial transfer from hMSCs to TC-1 cells. In addition, GFP-expressed TC-1 cells (GFP-TC-1) were prepared through the same lentivirus transfection methods and cocultured with MitoTracker Red CMXRos–labeled hMSCs (as described above) for quantitative measurements of the mitochondrial transfer rate using a flow cytometer. For the coculture system, TC-1 cells and hMSCs were cocultured at a cell number ratio of 3:1. For the Transwell test, 24-well Transwell plates (Corning Costar, Cambridge, USA), 6.5 mm in diameter with 0.4-μm pore membranes, were applied. The same number of TC-1 cells was plated on the lower chamber, and hMSCs at the same ratio (TC-1:hMSC = 3:1) were plated on the upper insert.

### Preparation of Cx43-silenced hMSCs

The down-regulation of Cx43 expression was performed by gene transfection of Cx43-siRNA (sense: AGGAAGAGAAACUGAACAATT; antisense: UUGUUCAGUUUCUCUUCCUTT). Briefly, LipoHigh liposomes were used to prepare the gene complexes carrying Cx43-siRNA following the manufacturer's instructions. The gene complexes were added to hMSCs in a serum-free culture medium for gene transfection. The culture medium was replaced by a serum-containing complete culture medium 3 hours after transfection. The transfection efficiency was assessed by Western blot analysis.

### Preparation of mtDNA-depleted hMSCs

The depletion of mtDNA of hMSCs was performed, according to a previous study (*48*). Briefly, hMSCs were cultured in the conditioned medium containing ethidium bromide (0.1 μg $ml^{-1}$), uridine (50 μg $ml^{-1}$), and 1 mM sodium pyruvate. After 4 weeks of continuous depletion, the mtDNA in hMSCs was measured by PCR assessments.

### Preparation of uniform IONPs

Uniform IONPs with a diameter of 20 nm were synthesized according to our previous study (*18*). Briefly, iron oleate complexes were initially prepared at 70°C for 4 hours. Afterward, these complexes were mixed with docosane and OA. The mixtures were then degassed at 100°C for 2 hours followed by continuously heating to 380°C at a heating rate of 3.3°C $min^{-1}$. After maintaining at this temperature for 3 min, the products were rapidly cooled down by acetone. The concentration of iron was assessed by inductively coupled plasma mass spectrometry (ICP-MS; XSeries 2, Thermo Fisher Scientific, Bremen, Germany). The hydrophilic surface modification containing OA-PCL/PEI was then performed following the methods used in our previous study (*34*). The morphology of synthesized IONPs was observed by TEM (JEM-2010, Tokyo, Japan).

### Preparation of MFION

The ferrimagnetic iron oxide nanocubes with the size of 25 nm were synthesized through the "heat-up" method and were self-assembled to MFION following the methods described in our previous study (*18*). The morphology of synthesized MFION was observed by TEM, and the concentration of iron was determined using ICP-MS.

### Quantification of iron amount by ICP-MS

hMSCs incubated with IONPs, ferrous irons, or ferric irons were washed by PBS thrice at an indicated time and then lysed by a

cell-lysing reagent. The lysed cells were collected and centrifuged at 10,000 rpm for 10 min. The supernatant of cell lysis solution was separated and acidized by concentrated nitric acid to dissolve the internalized iron. The mixture was heated using a heating plate at 200°C until the nitric acid was nearly evaporated. Then, the iron ions were dissolved with dilute nitric acid, and the iron amount was quantified by ICP-MS.

### Cx43 staining

The Cx43 expressions of hMSCs and Fe-hMSCs were observed using CLSM. Briefly, the stem cells were washed thrice and fixed by 4% paraformaldehyde for 15 min, followed by the treatment of 0.1% Triton X-100 for 30 min and goat serum for another 30 min. The diluent primary antibodies (human anti-Cx43 monoclonal antibody) were then added into cells for overnight incubation at 4°C, after which cells were incubated with a secondary antibody for 1 hour. Last, cells were washed by PBS thrice and incubated with DAPI for 8 min to visualize nuclei.

### Cx43 expression regulation by iron ions

hMSCs were seeded in culture dishes (30 mm in diameter; Sorfa Co. Ltd., Huzhou, China) beforehand for 24 hours. Ferric trichloride or ferrous sulfate at indicated concentrations (calculated by the iron amount) was dropped into the culture medium for 1 hour of coincubation. The Cx43 expression in hMSCs was then analyzed by Western blot.

### Western blot

Western blot analyses were preformed to assess the Cx43 and TGF-β expression in the present study. Briefly, cell samples were lysed in RIPA buffer containing protease inhibitor cocktail (5 μg $ml^{-1}$) and 1 mM phenylmethylsulfonyl fluoride. After centrifugation at 18,000*g* at 4°C for 10 min, the cell lysates were resolved by 10% SDS–polyacrylamide gel electrophoresis and proteins on gels were transferred to a polyvinylidene fluoride membrane (Millipore, Bedford, USA). The membrane was blocked with 5% BSA for 1 hour, followed by washing with PBS containing 0.1% Tween 20. The washed membrane was incubated overnight at 4°C with primary antibodies (human anti-Cx43 monoclonal antibody and mouse anti–TGF-β monoclonal antibody), followed by incubation with the secondary antibody (goat anti-rabbit antibody and goat anti-mouse antibody) for 1 hour at room temperature. The bands were visualized using an enhanced chemiluminescence kit (Millipore, Billerica, USA). Images were taken using Epson Perfection (V300 Photo, Epson, Nagano, Japan) and quantified densitometrically by AlphaEase FC software (Alpha Innotech, San Leandro, USA). The data were normalized to the level of GAPDH.

### Real-time observation of the intercellular transfer of mitochondria

The dynamics of the mitochondrial transfer from GFP-Fe-hMSCs toward BLM-TC-1 cells were monitored using CLSM. Briefly, GFP-Fe-hMSCs were prestained with a MitoTracker probe (MitoTracker Deep Red, 50 nM) for 30 min. BLM treatments were performed for 24 hours beforehand to induce the injury of the mCherry-TC-1 cells. The injured mCherry-TC-1 cells were harvested and cocultured with mitochondria-stained GFP-Fe-hMSCs at a humid atmosphere of 37°C and 5% $CO_2$. Images were taken every 5 min automatically and managed using the software (Leica LAS X, Leica, Wetzlar, Germany).

### Mitochondrial transfer rate quantified using flow cytometry

MitoTracker Red CMXRos–labeled hMSCs and GFP-TC-1 cells were first collected by trypsinization and subsequently washed twice with neutral PBS. Cell samples were resuspended in PBS for quantitative analysis using flow cytometry (BD Fortessa, BD Biosciences, San Jose, USA). GFP-TC-1 cells were gated, and the ratio of MitoTracker Red CMXRos–positive GFP-TC-1 cells was regarded as the transfer rate.

### Isolation of GFP-TC-1 cells from the coculture system

Briefly, all cells in the coculture system were collected by trypsinization and subsequently washed twice with neutral PBS. The GFP-positive TC-1 cells in the mixed cell samples were isolated using a fluorescence-activated sorting flow cytometer (MoFlo Astrios EQ, Beckman, Brea, USA). The FL1 channel (488 blue laser)–positive cells were gated and collected.

### Intracellular and mitochondrial ROS determination

For the intracellular ROS evaluation, 50 μM working solutions of DHE were added into the cell culture medium, followed by incubation at room temperature for 30 min. Cell samples were then washed with neutral PBS thrice and harvested for quantitative evaluation using flow cytometry. For the mitochondrial ROS detection, cell samples were stained using the MitoSOX red mitochondrial superoxide indicator (5 μM) for 10 min at 37°C. The stained cells were washed with HBSS thrice, and the positive cells were quantitatively analyzed by flow cytometry.

### Mitochondrial membrane potential measurements

The mitochondrial membrane potential was detected with a 5,5′,6,6′-tetrachloro-1,1′,3,3′- tetraethylbenzimidazole-carbocyanide iodine (JC-1) mitochondrial membrane potential kit (Yeasen, Shanghai, China) according to the manufacturer's instructions. Briefly, cell pellets were prepared after trypsinization of cell samples and subsequently incubated with JC-1 (10 μg $ml^{-1}$) for 15 min at 37°C with 5% $CO_2$. After washing with neutral PBS thrice, a flow cytometry analysis was performed. The monomeric form (damaged mitochondria) of JC-1 was detected in the FL1 channel, and the aggregated form of JC-1 was detected in the FL2 channel (healthy mitochondria).

### Cell apoptosis determination

Annexin V and propidium iodide (PI) staining in the apoptosis detection kit (Yeasen, Shanghai, China) was applied to determine apoptosis according to the manufacturer's instructions. Briefly, cell samples were collected by trypsinization and subsequently washed twice with precooled PBS twice. Cell samples were then collected by centrifugation and resuspended in 1× binding buffer (100 μl). Afterward, 5 μl of annexin V and 10 μl of PI were added into the cell suspension and incubated at room temperature for 15 min in a dark environment. The stained cells were diluted with 400 μl of 1× binding buffer followed by analysis using flow cytometry within 1 hour. The ratio of living somatic cells was obtained by counting the double-negative stained cells in the gated population and expressed as a percentage of the total cell count.

### Cellular proliferation assessments

Ethynyl deoxyuridine (EdU) cell proliferation detection kit (Beyotime, Shanghai, China) was used to assess the proliferation of TC-1

cells after indicted treatments. In short, prewarmed 2× EdU solutions were added into the adherent TC-1 cells, followed by incubation at 37°C with 5% $CO_2$ for 2 hours. Cells were subsequently fixed by 4% paraformaldehyde at room temperature for 15 min and incubated with 0.3% Triton X-100 at room temperature for 10 min. After washing thrice, cell samples were reacted with the Click Additive Solution at room temperature for 30 min in a dark environment, followed by another three washes. The quantitative evaluations were performed using flow cytometry analysis.

### Cell viability

The viability was determined with a CCK-8 assay kit (Beyotime, Shanghai, China) according to the manufacturer's instructions. Briefly, 40 μl of CCK-8 solutions was added to adherent cells, followed by incubation at 37°C with 5% $CO_2$ for 2 hours. The optical density (OD) was measured at 450 nm using a microplate reader (ELx800, BioTek Instruments, Winooski, USA).

### Intracellular ATP determination

The ATP levels were determined using an ATP assay kit (Beyotime, Shanghai, China) according to the manufacturer's instructions. Typically, the adherent cell samples were lysed, followed by centrifugation at 12,000*g* with 4°C for 5 min. After the collection of supernatants (20 μl), 100 μl of ATP working solutions was added to detect the light unit with a luminometer (GloMax, Promega, Madison, USA). The ATP concentration was calculated according to the calibration curve. The total amount of protein in each well was measured using a BCA protein assay reagent kit (Beyotime, Shanghai, China) to normalize the influence of the variation in the number of cells on the ATP concentration. The final intracellular ATP level was normalized as ATP concentration per cell protein.

### In vivo distribution of hMSCs and Fe-hMSCs

hMSCs and Fe-hMSCs were labeled with CM-Dil according to the method used in our previous study (*17*). These stem cells were intravenously administrated through the mice tail vein, with $3 \times 10^5$ cells per mouse. At the indicated time points, euthanasia of mice by deep anesthesia with 1% sodium pentobarbital was performed. Afterward, major organs, including brain, heart, lung, kidney, and spleen, were harvested and the distribution was examined by using an intravital fluorescent imaging system (MK50101-EX, Cambridge Research and Instrumentation, Woburn, USA).

For the micro-observation of the distribution in lungs, CM-Dil–labeled hMSCs or Fe-hMSCs were intravenously administrated as the same procedures described above. The lung samples were harvested and embedded in optimal cutting temperature compound (O.C.T. Compound, Tissue-Tek, Sakura, Torrance, USA) and cut into 6-μm-thick sections. AECs were visualized by immumohistochemical staining using an FITC-conjugated CK7 antibody; the nuclei were visualized by staining with DAPI (100 ng $ml^{-1}$). In addition, the distribution of Fe-hMSCs in lungs was further examined by Prussian blue staining used the method described in our previous report (*18*).

### Collection of BALF

BALF was collected following the methods used in the previous study (*49*). Briefly, the mice were euthanized before tracheal cannula, followed by lung lavage with 1 ml of saline thrice. The collected BALF was stored on ice before the determination.

### Enzyme-linked immunosorbent assay

The amounts of MMP9 and TGF-β in BALF were determined by enzyme-linked immunosorbent assay (ELISA) kits (Boster, Wuhan, China) following the manufacturer's protocol. The collected BALF in 96-wells plates was incubated at 37°C for 90 min, followed by incubation with antibodies of MMP9 and TGF-β at 37°C for 60 min. After washing with neutral PBS thrice, avidin-peroxidase complex was added, followed by further incubation at 37°C for 30 min. Subsequently, the samples were washed by using neutral PBS five times, and 3,3′,5,5′-tetramethyl benaidine (TMB substrate) was added for chromogenic reactions at 37°C for 20 min. After the termination of the reactions, the OD value was measured at 450 nm using a microplate reader.

### Histological assessments of lung sections

The lung samples were fixed in 4% formaldehyde solution, subsequently embedded in paraffin, and cut into 6-μm-thick sections. Both H&E staining and Masson's trichrome staining were performed. The images were taken using a Panoramic MIDI slide scanner (3DHISTECH Kft., Budapest, Hungary). Collagen depositions were quantified by counting the ratio of fibrotic area according to the Masson's trichrome section using ImageJ (ij152-win-java8, National Institutes of Health, Bethesda, USA).

### MDA determination

Typically, mice were euthanized by deep anesthesia with 1% sodium pentobarbital, and lung samples were harvested carefully. Fresh lung samples of 100 mg were homogenized into 10% homogenate with 1 ml of precooled reagent A, followed by centrifugation at 12,000*g* for 5 min. A proportion of homogenizer supernatants (0.2 ml) were taken out and added into 0.2 ml of reagent B, 1.5 ml of reagent C, 1.5 ml of reagent D of MDA detection kit, and 1 ml of double-distilled water. The mixed solutions were heated in a boiling water bath for 50 min and then were quickly cooled in ice water. The mixed solutions were centrifuged at 3000 rpm at 4°C for 15 min. The MDA contents of the supernatants were measured with an ultraviolet spectrophotometer (TU-1900, Persee, Beijing, China) at 532 nm.

### SOD determination

Fresh lung tissues (100 mg) harvested as described above were grinded into 10% homogenate by 1 ml of precooled normal saline. The homogenate was centrifuged at 12,000*g* for 5 min, and the supernatants were mixed with subsequent A, B, C, and D solutions of the SOD detection kit. The mixed solutions were heated in a 37°C water bath for 50 min, followed by reaction with color development reagent for 10 min. The SOD contents of the supernatants were measured with an ultraviolet spectrophotometer at 550 nm.

### Hydroxyproline evaluation

Briefly, lung samples harvested as described above were cut into pieces and subsequently dissolved by acid hydrolysis at 110°C for 6 hours. The solutions were centrifuged at 16,000 rpm with 25°C for 20 min, and the collected supernatants were neutralized by sodium hydroxide. The concentration of hydroxyproline in the supernatants was assessed by the hydroxyproline detection kit (Solarbio, Beijing, China) according to the manufacturer's instructions, and the OD values were measured at 560 nm using an ultraviolet spectrophotometer.

### Micro-CT scanning

Mice were anaesthetized by halothane and then imaged with a small-animal micro-CT scanner (U-CT-XUHR, MILabs, Houten, The Netherlands). The x-ray system of the scanner applied a micro-focus tube in an accurate mode, with a voltage of 50 kV, a current of 0.21 mA, and an exposure time of 75 ms. The projection radiographs were taken throughout the 360° gantry rotation for a total scan time of 5 to 10 min.

### Biological transmission electron microscopy

Typically, cell samples or lung samples were fixed with 4% precooled glutaraldehyde overnight at 4°C, followed by PBS washing the next day. Subsequently, a series of treatments on the samples by 1% osmic acid fixation, water wash, 2% uranyl acetate staining, gradient concentration ethanol, and acetone dehydration were performed. Afterward, the dehydrated samples were embedded in Epon 812 gelatin and sliced into 100-nm samples. The morphologies of mitochondria were then observed with TEM (Tecnai G2 spirit, Thermo Fisher Scientific, Bremen, Germany).

### Isolation of AECs from lung samples

Briefly, lung samples were harvested as described above, followed by dissolving in the PBS solution containing collagenase (2 mg $ml^{-1}$) and deoxyribonuclease I (50 U $ml^{-1}$) for 40 min. Cell suspensions were then centrifuged twice at 2800 rpm at 4°C and, each time, for 5 min to harvest the precipitates. The obtained precipitates were resuspended in 1% BSA (100 μl) containing CD31, CD45, and CD326 antibodies and incubated at 4°C for 30 min in a dark environment. After an extra centrifugation, AECs were sorted from the cell precipitates by using a fluorescence-activated sorting flow cytometer. Cells with the surface marker of $CD31^{-}CD45^{-}CD326^{+}$ were collected for further PCR tests.

### Isolation of mitochondria

Adherent hMSCs were collected by trypsinization and resuspended in 1 ml of precooled lysis buffer. The cell suspension was transferred into a small-volume glass homogenizer and ground 30 times within ice bath. The supernatant was collected by centrifugation at 1000*g* at 4°C for 5 min twice, followed by further centrifugation of the collected supernatant at 12,000*g* at 4°C for 10 min to obtain the crude mitochondrial precipitation. These obtained mitochondrial precipitations were then resuspended by 50 μl of wash buffer and centrifuged at 1000*g* at 4°C for 5 min. Last, the supernatant was collected after another centrifugation at 12,000*g* at 4°C for 10 min to obtain mitochondrial precipitation with high purity. These obtained mitochondrial precipitations were resuspended in store buffer and used immediately.

### Human mtDNA measurements using PCR

The human mitochondrial copy number of isolated AECs from mice lungs was measured by PCR analysis. The primers of human-specific mtDNA applied in the present study were 5′-CCCCACAAACCCCATTACTAAACCCA-3′ (forward) and 5′-TTTCATCATGCGGAGATGTTGGATGG-3′ (reverse) and those of human nuclear β-globin DNA (nDNA) were 5′-GAAGAGCCAAGGACAGGTAC-3′ (forward) and 5′-GGAAAATAGACCAATAGGCAG-3′ (reverse). The relative human mtDNA copy numbers in isolated AECs were quantified by $2^{-(\Delta\Delta Ct)}$ by real-time PCR [StepOnePlus, ABI (Applied Biosystems), Foster, USA]. All the samples were detected in triplicate.

### Mice PF model

Male C57BL/6 mice (18 to 22 g) were used to prepare the PF model according to previous studies (*33*, *44*). BLM was dissolved in PBS and intratracheally administered at a dose of 0.02 mg in 50 μl of PBS per mouse. All animal studies were approved by the Animal Experimental Ethics Committee of the Zhejiang University and performed in accordance with the committee's guidelines on animal handling.

### In vivo PF treatment

hMSCs with indicated treatments were intravenously administered to PF mice through the tail vein on the following day after the intratracheal instillation of BLM, with $5 \times 10^5$ cells per mouse injected. For the free mitochondria treatment group (hMSC-mito), mitochondria isolated from $1.5 \times 10^6$ hMSCs were intratracheally injected per mouse. To compare the therapeutic outcomes of this strategy on PF mice with different degrees of fibrosis, hMSCs and Fe-hMSCs were administrated intravenously to PF mice 7 and 14 days after BLM injection. The survival of mice after each treatment was monitored every day. After the 28-day treatment period, the mice were scanned using micro-CT after performing euthanasia by halothane. BALF was harvested for biochemical tests of TGF-β and MMP9. In addition, lung samples were extracted for further pathological examinations and homogenate preparation. Concentrations of SOD, MDA, and hydroxyproline in lung homogenates were assessed using the relevant kit according to the manufacturer's instructions as described above.

### Observations of the intercellular transfer of mitochondria in vivo

Mitochondria of hMSCs, Fe-hMSCs, and shMSCs were prestained with MitoTracker Red CMXRos before intravenous administration to PF mice. Mice lungs were harvested 24 hours after the stem cell administration to prepare the sections. AECs were visualized by immunofluorescence staining using a Cy5-conjugated CK7 antibody. All cell nuclei were stained by DAPI. PF model mice without cell administrations were used as blank controls. The mitochondrial transfer from stem cells toward AECs was examined by CLSM. In addition, mice AECs were separated using flow cytometry, and the number of human mtDNA in AECs was quantitatively measured by PCR evaluations.

### Statistical analysis

All statistical analyses were conducted using GraphPad Prism version 8.2.1 (GraphPad Software; www.graphpad.com). Data of the tests that were performed in triplicate or over three times were expressed as the mean value ± SD. For assessing differences between the two groups, an unpaired Student's *t* test was performed. For determining differences among multiple groups, a one-way analysis of variance (ANOVA) was used. For determining differences between the two groups based on two independent variables, a two-way ANOVA was used. *P* values <0.05 were considered statistically significant; *P* values <0.01 were considered very statistically significant.

## SUPPLEMENTARY MATERIALS

Supplementary material for this article is available at https://science.org/doi/10.1126/sciadv.abg0534

## REFERENCES AND NOTES

1. R. J. Youle, A. M. van der Bliek, Mitochondrial fission, fusion, and stress. *Science* **337**, 1062–1065 (2012).

2. J. A. Nicolás-Ávila, A. V. Lechuga-Vieco, L. Esteban-Martinez, M. Sanchez-Diaz, E. Diaz-Garcia, D. J. Santiago, A. Rubio-Ponce, J. L. Li, A. Balachander, J. A. Quintana, R. Martínez-de-Mena, B. Castejón-Vega, A. Pun-Garcia, P. G. Traves, E. Bonzon-Kulichenko, F. Garcia-Marques, L. Cussó, N. A-González-Guerra, M. Roche-Molina, S. Martin-Salamanca, G. Crainiciuc, G. Guzman, J. Larrazabal, E. Herrero-Galan, J. Alegre-Cebollada, G. Lemke, C. V. Rothlin, L. J. Jimenez-Borreguero, G. Reyes, A. Castrillo, M. Desco, P. Muñoz-Cánoves, B. Ibáñez, M. Torres, L. G. Ng, S. G. Priori, H. Bueno, J. Vázquez, M. D. Cordero, J. A. Bernal, J. A. Enriquez, A. Hidalgo, A network of macrophages supports mitochondrial homeostasis in the heart. *Cell* **183**, 94–109.e23 (2020).
3. M. N. Islam, S. R. Das, M. T. Emin, M. Wei, L. Sun, K. Westphalen, D. J. Rowlands, S. K. Quadri, S. Bhattacharya, J. Bhattacharya, Mitochondrial transfer from bone-marrow-derived stromal cells to pulmonary alveoli protects against acute lung injury. *Nat. Med.* **18**, 759–765 (2012).
4. K. Hayakawa, E. Esposito, X. Wang, Y. Terasaki, Y. Liu, C. Xing, X. Ji, E. H. Lo, Transfer of mitochondria from astrocytes to neurons after stroke. *Nature* **535**, 551–555 (2016).
5. E. F. Fang, Y. Hou, K. Palikaras, B. A. Adriaanse, J. S. Kerr, B. Yang, S. Lautrup, M. M. Hasan-Olive, D. Caponio, X. Dan, P. Rocktaschel, D. L. Croteau, M. Akbari, N. H. Greig, T. Fladby, H. Nilsen, M. Z. Cader, M. P. Mattson, N. Tavernarakis, V. A. Bohr, Mitophagy inhibits amyloid-β and tau pathology and reverses cognitive deficits in models of Alzheimer's disease. *Nat. Neurosci.* **22**, 401–412 (2019).
6. A. Caicedo, P. M. Aponte, F. Cabrera, C. Hidalgo, M. Khoury, Artificial mitochondria transfer: Current challenges, advances, and future applications. *Stem Cells Int.* **2017**, 7610414 (2017).
7. M. Picard, T. Taivassalo, D. Ritchie, K. J. Wright, M. M. Thomas, C. Romestaing, R. T. Hepple, Mitochondrial structure and function are disrupted by standard isolation methods. *PLOS ONE* **6**, e18317 (2011).
8. J. L. Gollihue, A. G. Rabchevsky, Prospects for therapeutic mitochondrial transplantation. *Mitochondrion* **35**, 70–79 (2017).
9. D. Jiang, F. X. Chen, H. Zhou, Y. Y. Lu, H. Tan, S. J. Yu, J. Yuan, H. Liu, W. Meng, Z. B. Jin, Bioenergetic crosstalk between mesenchymal stem cells and various ocular cells through the intercellular trafficking of mitochondria. *Theranostics* **10**, 7260–7272 (2020).
10. T. Ahmad, S. Mukherjee, B. Pattnaik, M. Kumar, S. Singh, M. Kumar, R. Rehman, B. K. Tiwari, K. A. Jha, A. P. Barhanpurkar, M. R. Wani, S. S. Roy, U. Mabalirajan, B. Ghosh, A. Agrawal, Miro1 regulates intercellular mitochondrial transport & enhances mesenchymal stem cell rescue efficacy. *EMBO J.* **33**, 994–1010 (2014).
11. V. A. Babenko, D. N. Silachev, V. A. Popkov, L. D. Zorova, I. B. Pevzner, E. Y. Plotnikov, G. T. Sukhikh, D. B. Zorov, Miro1 enhances mitochondria transfer from multipotent mesenchymal stem cells (MMSC) to neural cells and improves the efficacy of cell recovery. *Molecules* **23**, 687 (2018).
12. H. Li, C. Wang, T. He, T. Zhao, Y. Y. Chen, Y. L. Shen, X. Zhang, L. L. Wang, Mitochondrial transfer from bone marrow mesenchymal stem cells to motor neurons in spinal cord injury rats via gap junction. *Theranostics* **9**, 2017–2035 (2019).
13. J. L. Spees, S. D. Olson, M. J. Whitney, D. J. Prockop, Mitochondrial transfer between cells can rescue aerobic respiration. *Proc. Natl. Acad. Sci. U.S.A.* **103**, 1283–1288 (2006).
14. M. V. Jackson, T. J. Morrison, D. F. Doherty, D. F. McAuley, M. A. Matthay, A. Kissenpfennig, C. M. O'Kane, A. D. Krasnodembskaya, Mitochondrial transfer via tunneling nanotubes is an important mechanism by which mesenchymal stem cells enhance macrophage phagocytosis in the in vitro and in vivo models of ARDS. *Stem Cells* **34**, 2210–2223 (2016).
15. C. T. Chen, Y. R. Shih, T. K. Kuo, O. K. Lee, Y. H. Wei, Coordinated changes of mitochondrial biogenesis and antioxidant enzymes during osteogenic differentiation of human mesenchymal stem cells. *Stem Cells* **26**, 960–968 (2008).
16. T. Y. Zhang, B. Huang, Z. Y. Yuan, Y. L. Hu, Y. Tabata, J. Q. Gao, Gene recombinant bone marrow mesenchymal stem cells as a tumor-targeted suicide gene delivery vehicle in pulmonary metastasis therapy using non-viral transfection. *Nanomedicine* **10**, 257–267 (2014).
17. T. Y. Zhang, B. Huang, H. B. Wu, J. H. Wu, L. M. Li, Y. X. Li, Y. L. Hu, M. Han, Y. Q. Shen, Y. Tabata, J. Q. Gao, Synergistic effects of co-administration of suicide gene expressing mesenchymal stem cells and prodrug-encapsulated liposome on aggressive lung melanoma metastases in mice. *J. Control. Release* **209**, 260–271 (2015).
18. T. Y. Zhang, F. Y. Li, Q. H. Xu, Q. Y. Wang, X. C. Jiang, Z. Y. Liang, H. W. Liao, X. L. Kong, J. A. Liu, H. H. Wu, D. P. Zhang, C. H. An, L. Dong, Y. Lu, H. C. Cao, D. Kim, J. H. Sun, T. Hyeon, J. Q. Gao, D. S. Ling, Ferrimagnetic nanochains-based mesenchymal stem cell engineering for highly efficient post-stroke recovery. *Adv. Funct. Mater.* **29**, 1900603 (2019).
19. M. Mahrouf-Yorgov, L. Augeul, C. C. Da Silva, M. Jourdan, M. Rigolet, S. Manin, R. Ferrera, M. Ovize, A. Henry, A. Guguin, J. P. Meningaud, J. L. Dubois-Rande, R. Motterlini, R. Foresti, A. M. Rodriguez, Mesenchymal stem cells sense mitochondria released from damaged cells as danger signals to activate their rescue properties. *Cell Death Differ.* **24**, 1224–1238 (2017).
20. S. Paliwal, R. Chaudhuri, A. Agrawal, S. Mohanty, Regenerative abilities of mesenchymal stem cells through mitochondrial transfer. *J. Biomed. Sci.* **25**, 31 (2018).
21. T. Zhang, Q. Xu, T. Huang, D. Ling, J. Gao, New insights into biocompatible iron oxide nanoparticles: A potential booster of gene delivery to stem cells. *Small* **16**, e2001588 (2020).
22. J. Han, B. Kim, J. Y. Shin, S. Ryu, M. Noh, J. Woo, J. S. Park, Y. Lee, N. Lee, T. Hyeon, D. Choi, B. S. Kim, Iron oxide nanoparticle-mediated development of cellular gap junction crosstalk to improve mesenchymal stem cells' therapeutic efficacy for myocardial infarction. *ACS Nano* **9**, 2805–2819 (2015).
23. Y. Yao, X. L. Fan, D. Jiang, Y. Zhang, X. Li, Z. B. Xu, S. B. Fang, S. Chiu, H. F. Tse, Q. Lian, Q. L. Fu, Connexin 43-mediated mitochondrial transfer of iPSC-MSCs alleviates asthma inflammation. *Stem Cell Rep.* **11**, 1120–1135 (2018).
24. D. J. Lederer, F. J. Martinez, Idiopathic pulmonary fibrosis. *N. Engl. J. Med.* **378**, 1811–1823 (2018).
25. F. J. Martinez, H. R. Collard, A. Pardo, G. Raghu, L. Richeldi, M. Selman, J. J. Swigris, H. Taniguchi, A. U. Wells, Idiopathic pulmonary fibrosis. *Nat. Rev. Dis. Primers.* **3**, 17074 (2017).
26. L. Richeldi, H. R. Collard, M. G. Jones, Idiopathic pulmonary fibrosis. *Lancet* **389**, 1941–1952 (2017).
27. E. Vasarmidi, E. Tsitoura, D. A. Spandidos, N. Tzanakis, K. M. Antoniou, Pulmonary fibrosis in the aftermath of the COVID-19 era (Review). *Exp. Ther. Med.* **20**, 2557–2560 (2020).
28. R. Crisan-Dabija, C. A. Pavel, I. V. Popa, A. Tarus, A. Burlacu, "A chain only as strong as its weakest link": An up-to-date literature review on the bidirectional interaction of pulmonary fibrosis and COVID-19. *J. Proteome Res.* **19**, 4327–4338 (2020).
29. W. Merkt, M. Bueno, A. L. Mora, D. Lagares, Senotherapeutics: Targeting senescence in idiopathic pulmonary fibrosis. *Semin. Cell Dev. Biol.* **101**, 104–110 (2020).
30. E. S. Malsin, D. W. Kamp, The mitochondria in lung fibrosis: Friend or foe? *Transl. Res.* **202**, 1–23 (2018).
31. S. W. Ryter, I. O. Rosas, C. A. Owen, F. J. Martinez, M. E. Choi, C. G. Lee, J. A. Elias, A. M. K. Choi, Mitochondrial dysfunction as a pathogenic mediator of chronic obstructive pulmonary disease and idiopathic pulmonary fibrosis. *Ann. Am. Thorac. Soc.* **15**, S266–S272 (2018).
32. J. Saleh, C. Peyssonnaux, K. K. Singh, M. Edeas, Mitochondria and microbiota dysfunction in COVID-19 pathogenesis. *Mitochondrion* **54**, 1–7 (2020).
33. G. Yu, A. Tzouvelekis, R. Wang, J. D. Herazo-Maya, G. H. Ibarra, A. Srivastava, J. P. W. de Castro, G. Deluliis, F. Ahangari, T. Woolard, N. Aurelien, E. D. R. Arrojo, Y. Gan, M. Graham, X. Liu, R. J. Homer, T. S. Scanlan, P. Mannam, P. J. Lee, E. L. Herzog, A. C. Bianco, N. Kaminski, Thyroid hormone inhibits lung fibrosis in mice by improving epithelial mitochondrial function. *Nat. Med.* **24**, 39–49 (2018).
34. Q. Xu, T. Zhang, Q. Wang, X. Jiang, A. Li, Y. Li, T. Huang, F. Li, Y. Hu, D. Ling, J. Gao, Uniformly sized iron oxide nanoparticles for efficient gene delivery to mesenchymal stem cells. *Int. J. Pharm.* **552**, 443–452 (2018).
35. M. J. Turk, J. A. Reddy, J. A. Chmielewski, P. S. Low, Characterization of a novel pH-sensitive peptide that enhances drug release from folate-targeted liposomes at endosomal pHs. *Biochim .Biophys. Acta* **1559**, 56–68 (2002).
36. K. Li, Y. Chi, K. Gao, Q. Yan, H. Matsue, M. Takeda, M. Kitamura, J. Yao, Connexin43 hemichannel-mediated regulation of connexin43. *PLOS ONE* **8**, e58057 (2013).
37. J. Y. Hahn, H. J. Cho, H. J. Kang, T. S. Kim, M. H. Kim, J. H. Chung, J. W. Bae, B. H. Oh, Y. B. Park, H. S. Kim, Pre-treatment of mesenchymal stem cells with a combination of growth factors enhances gap junction formation, cytoprotective effect on cardiomyocytes, and therapeutic efficacy for myocardial infarction. *J. Am. Coll. Cardiol.* **51**, 933–943 (2008).
38. G. Mese, G. Richard, T. W. White, Gap junctions: Basic structure and function. *J. Invest. Dermatol.* **127**, 2516–2524 (2007).
39. T. W. White, D. L. Paul, Genetic diseases and gene knockouts reveal diverse connexin functions. *Annu. Rev. Physiol.* **61**, 283–310 (1999).
40. A. Averyanov, I. Koroleva, M. Konoplyannikov, V. Revkova, V. Lesnyak, V. Kalsin, O. Danilevskaya, A. Nikitin, A. Sotnikova, S. Kotova, V. Baklaushev, First-in-human high-cumulative-dose stem cell therapy in idiopathic pulmonary fibrosis with rapid lung function decline. *Stem Cells Transl. Med.* **9**, 6–16 (2020).
41. S. Rangarajan, K. Bernard, V. J. Thannickal, Mitochondrial dysfunction in pulmonary fibrosis. *Ann. Am. Thorac. Soc.* **14**, S383–S388 (2017).
42. S. C. Abreu, M. A. Antunes, P. Pelosi, M. M. Morales, P. R. Rocco, Mechanisms of cellular therapy in respiratory diseases. *Intensive Care Med.* **37**, 1421–1431 (2011).
43. M. K. Glassberg, J. Minkiewicz, R. L. Toonkel, E. S. Simonet, G. A. Rubio, D. DiFede, S. Shafazand, A. Khan, M. V. Pujol, V. F. LaRussa, L. H. Lancaster, G. D. Rosen, J. Fishman, Y. N. Mageto, A. Mendizabal, J. M. Hare, Allogeneic human mesenchymal stem cells in patients with idiopathic pulmonary fibrosis via intravenous delivery (AETHER): A phase I safety clinical trial. *Chest* **151**, 971–981 (2017).
44. T. Liu, F. G. De Los Santos, S. H. Phan, The bleomycin model of pulmonary fibrosis. *Methods Mol. Biol.* **1627**, 27–42 (2017).
45. A. Rustom, R. Saffrich, I. Markovic, P. Walther, H. H. Gerdes, Nanotubular highways for intercellular organelle transport. *Science* **303**, 1007–1010 (2004).
46. E. J. Benjamin, S. S. Virani, C. W. Callaway, A. M. Chamberlain, A. R. Chang, S. Cheng, S. E. Chiuve, M. Cushman, F. N. Delling, R. Deo, S. D. de Ferranti, J. F. Ferguson, M. Fornage, C. Gillespie, C. R. Isasi, M. C. Jimenez, L. C. Jordan, S. E. Judd, D. Lackland, J. H. Lichtman, L. Lisabeth, S. Liu, C. T. Longenecker, P. L. Lutsey, J. S. Mackey,

D. B. Matchar, K. Matsushita, M. E. Mussolino, K. Nasir, M. O'Flaherty, L. P. Palaniappan, A. Pandey, D. K. Pandey, M. J. Reeves, M. D. Ritchey, C. J. Rodriguez, G. A. Roth, W. D. Rosamond, U. K. A. Sampson, G. M. Satou, S. H. Shah, N. L. Spartano, D. L. Tirschwell, C. W. Tsao, J. H. Voeks, J. Z. Willey, J. T. Wilkins, J. H. Wu, H. M. Alger, S. S. Wong, P. Muntner; American Heart Association Council on Epidemiology; Prevention Statistics Committee; Stroke Statistics Subcommittee, Heart disease and stroke statistics-2018 update: A report from the American Heart Association. *Circulation* **137**, e67–e492 (2018).

47. H. Cao, J. Yang, J. Yu, Q. Pan, J. Li, P. Zhou, Y. Li, X. Pan, J. Li, Y. Wang, L. Li, Therapeutic potential of transplanted placental mesenchymal stem cells in treating Chinese miniature pigs with acute liver failure. *BMC Med.* **10**, 56 (2012).
48. R. Burt, A. Dey, S. Aref, M. Aguiar, A. Akarca, K. Bailey, W. Day, S. Hooper, A. Kirkwood, K. Kirschner, S. W. Lee, C. Lo Celso, J. Manji, M. R. Mansour, T. Marafioti, R. J. Mitchell, R. C. Muirhead, K. C. Y. Ng, C. Pospori, I. Puccio, K. Zuborne-Alapi, E. Sahai, A. K. Fielding, Activated stromal cells transfer mitochondria to rescue acute lymphoblastic leukemia cells from oxidative stress. *Blood* **134**, 1415–1429 (2019).
49. D. I. Kim, M. K. Song, H. I. Kim, K. M. Han, K. Lee, Diesel exhaust particulates induce neutrophilic lung inflammation by modulating endoplasmic reticulum stress-mediated cxcl1/kc expression in alveolar macrophages. *Molecules* **25**, 6046 (2020).

**Acknowledgments:** We would like to thank P. Luo from Institute of Pharmacology and Toxicology, College of Pharmaceutical Sciences, Zhejiang University for mouse AECs (TC-1 cells). We also thank T. Hao at Analysis and Measurement Center of Zhejiang University and the Center of Cryo-Electron Microscopy (CCEM), Zhejiang University for technical assistance on TEM. **Funding:** This work was funded by the National Natural Science Foundation of China (nos. 81620108028, 81703423, and 81973252), China Postdoctoral Science Foundation (2018M640568 and 2016M601938), Ten-thousand Talents Program of Zhejiang Province (2018R52049), and the Fundamental Research Funds for the Central Universities (2021FZZX001-46). **Author contributions:** T.Z., Z.G., and J.G. conceived the project and designed the experiments. T.H. and T.Z. carried out all the experiments. X.J., H.W., R.L., and N.L. assisted the cell experiments. A.L., Y.S., and Q.B. assisted in the animal studies and the safety evaluations. H.C. harvested hMSCs and instructed the stem cell experiments. D.L. instructed the preparation of magnetic iron nanoparticles. Y.T. instructed the whole studies. T.Z., T.H., and J.G. wrote the manuscript. J.W. revised the manuscript. X.J. polished the figures. Z.G. and J.G. discussed the results and commented on the manuscript. All authors discussed the results and commented on the manuscript. **Competing interests:** Z.G. is a scientific cofounder of ZenCapsule and ZCapsule. The other authors declare no competing interests. **Data and materials availability:** All data needed to evaluate the conclusions in the paper are present in the paper and/or the Supplementary Materials.

Submitted 18 April 2021
Accepted 30 July 2021
Published 29 September 2021
10.1126/sciadv.abj0534

**Citation:** T. Huang, T. Zhang, X. Jiang, A. Li, Y. Su, Q. Bian, H. Wu, R. Lin, N. Li, H. Cao, D. Ling, J. Wang, Y. Tabata, Z. Gu, J. Gao, Iron oxide nanoparticles augment the intercellular mitochondrial transfer–mediated therapy. *Sci. Adv.* **7**, eabj0534 (2021).